This document contains the draft version of the following paper:

T. Peng, A. Balijepalli, S.K. Gupta, and T. LeBrun. Algorithms for on-line monitoring of micro-spheres in an optical tweezers-based assembly cell. *ASME Journal of Computing and Information Science in Engineering*, 7(4):330-338, 2007.

Readers are encouraged to get the official version from the journal's web site or by contacting Dr. S.K. Gupta (skgupta@umd.edu).

Algorithms for On-Line Monitoring of Micro-Spheres in an Optical Tweezers-Based Assembly Cell

Tao Peng[1], Arvind Balijepalli[2], Satyandra K Gupta[3], and Tom LeBrun[4]

Abstract

Optical tweezers have emerged as a powerful tool for micro and nanomanipulation. Using optical tweezers to perform automated assembly requires on-line monitoring of components in the assembly workspace. This paper presents algorithms for estimating 3-dimensional positions of micro-spheres in the assembly workspace. Algorithms presented in this paper use images obtained by optical section microscopy. The images are first segmented to locate areas of interest and then image gradient information from the areas of interest is used to locate the positions of individual micro-spheres in the XY-plane. Finally, signature curves are computed and utilized to obtain the Z-locations of spheres. We have tested these algorithms with glass micro-spheres of two different sizes under different illumination conditions. Our experiments indicate that the algorithms described in this paper provide sufficient computational speed and accuracy to support the operation of optical tweezers.

Keywords: On-Line Monitoring, Position Estimation, and Image Analysis.

1. Introduction

Light beams exert small forces on objects, and for objects smaller than tens of micrometers the forces can be designed to "grasp" a particle in an optical beam and move it to a desired position. Using this property of light beams, optical tweezers have been developed to successfully trap and move nanoscale and microscale components of different sizes and shapes [Agar05, Ashk86, Ashk00, Pauz06, Svob94, Yu04]. Optical tweezers provide a broad range of positioning and orienting capabilities to place components at the desired locations in the workspace. By utilizing multiple lasers beams, optical tweezers can perform several operations in parallel. These characteristics make optical tweezers a very promising technology for micro and nanomanipulation.

Currently optical tweezers are operated by highly experienced human operators and performing a single successful assembly operation can take days of effort. In order to use optical tweezers in production processes, the following fundamental advances are needed:

[1] Mechanical Engineering Department, University of Maryland
[2] Mechanical Engineering Department, University of Maryland and Manufacturing Engineering Laboratory, National Institute of Standards and Technology
[3] Mechanical Engineering Department and Institute for Systems Research, University of Maryland
[4] Manufacturing Engineering Laboratory, National Institute of Standards and Technology

- The overall speed of assembly has to increase considerably to ensure that operations can be performed cost effectively.

- The overall yield of assembly operations should increase significantly to ensure that a large number of assembly operations could be performed without encountering significant assembly errors.

- The reliance on highly trained human operators must decrease to facilitate wide spread use of this technology.

To address the above challenges, we are developing an optical tweezers based assembly instrument [Bali06, Gorm05]. Components used in the assembly process are added to a fluid medium that is injected into the cell. The concentration of components in the cell is controlled to ensure that the assembly will be viable despite any losses during the component insertion process. Components used in the assembly operation are moved to a kitting area using the trap laser. We are able to simultaneously hold many components by time sharing a single laser beam, so the components in the kitting area are held by individually controlled traps. The next step is to clear the assembly area by moving all the spare components to a recycling area. After this step, the components are transferred from the kitting area to the assembly area and the actual assembly begins. The partially completed assembly can then be preserved by attaching it to a surface or transporting it for further processing or collection using microfluidics. The method of attachment to the substrate can range from Van der Walls forces to adhesive surface chemistry or even incorporating active MEMS based fixtures. After the assembly has been completed, the detachable assembly substrate, typically a perfusion chamber, can be removed and the finished assembly transferred to the next step in the fabrication process, such as critical point drying.

Assembly tasks are typically performed in a fluidic medium and components that are not trapped constantly move in an unpredictable manner due to Brownian motion. Hence it is not possible to know a priori the positions and orientations of components in the assembly cell. Achieving higher levels of automation in the assembly process requires knowledge of the component locations during the assembly operation. Therefore, we need a 3-D vision system to recognize the component using optical microscopy of microscale components. Figure 1 shows the 3-D imaging setup in detail. The imaging module, which consists of software that controls the microscope focus as well as the camera, can focus the microscope to different heights in the assembly cell and generate a stack of images in one scanning cycle. Each image is captured with plane of focus of the microscope at a different height in the assembly cell, and by analyzing one image stack a 3-D model of the assembly cell can be built. (We use the terms “plane of focus” to avoid confusion with “focal plane” which has a different meaning. This is also called the object plane or specimen plane.) This task requires new algorithms for estimating positions, orientations, and sizes of components.

The estimation algorithms will need to be designed to address the following three challenges:

- For imaging at microscopic scales, resolving 3-D positions of objects from analysis of 2-D images is a challenging problem due to limited resolution of imaging techniques and optical effects observed at small length scales.

- The 3-D workspace contains a large number of components which move constantly due to Brownian motion. Components may come close to each other in the workspace and hence occlude each other. The estimation algorithms should be able to resolve such a complex scene of 3-D components.

- To achieve autonomy, we will need an on-line monitoring system that can measure, construct and update the positions of components in the 3-D workspace at a rate sufficient to allow interactive assembly. Our initial target is to achieve an update rate of 20Hz.

Micro-spheres are important building blocks and are used in many applications including photonics, grippers for cell manipulation, and templates for self assembly. This paper presents algorithms for estimating positions of micro-spheres in the 3-D assembly workspace using images obtained by optical section microscopy. Images are first segmented to locate the areas of interest in the section. Then, image gradient information extracted from the areas of interest is used to locate the positions of micro-spheres in the XY-plane. Finally, signature curves, which relate the image pattern of a sphere to its distance from the plane of focus are computed and utilized to obtain the Z-locations. We have tested these algorithms with glass micro-spheres under varied illumination conditions.

2. Related Work

A popular method used to study 3D microscopic structures is optical sectioning with the use of confocal microscopes [Brak89, Wils89]. A confocal microscope is able to reject light from objects out of the plane of focus better than conventional light microscopes. Because of this, a confocal microscope can perform excellent optical sectioning of a sample and capture views of very thin cross-sections. By scanning the sample vertically, a stack of cross-sections of the sample can be acquired. These cross-sections can be combined to give a voxel-based representation of the 3-D structure of sample. This optical sectioning technique with the use of confocal microscopes has been widely used in biological, chemical and medical studies [Fred99]. However, the acquisition of a voxel-based representation requires fine scanning of the sample, which can take considerable time and generate large data sets. Geometric analysis and visualization of such voxel-based representations is computationally expensive [Luca96, Clen02]. Also, given that confocal microscopes are generally slower than conventional microscopes in capturing images, their use in optical sectioning is limited to studies of static or slowly changing phenomenon.

Acquisition of volumetric data with confocal microscopes is a great tool to study complex 3-D structures and scenes at microscopic scales. For simpler 3-D structures or scenes, a volumetric representation may not be necessary and less demanding methods can be used. Crocker and Grier [Croc96] developed a set of imaging processing algorithms for their colloidal studies, in which the 3-D locations of individual colloidal spheres can be determined from a single image. The computation of the XYZ position of a sphere was based on the intensity distribution of the sphere's image, e.g. the centroid of the intensity distribution was taken as the XY position (position inside the image plane) of the sphere and the Z-position was calculated from the moments of the intensity distribution. By using this method, the scanning process for the

workspace is abandoned, which makes the reconstruction of the 3-D scene much faster and the colloidal spheres in the workspace can be traced in real-time [Week00].

In our work we are dealing with components with a simple geometric shape but in a relatively complex scene, i.e. a possibly large number of components spread throughout the 3-D workspace in a disordered manner moving constantly and potentially clustered with each other. In such case, the method developed by Crocker and Grier cannot be used because it is unable to discriminate clustered spheres and has a limited imaging range along Z-direction. Therefore we chose to use an optical sectioning scheme that relies on images collected by scanning the microscope's plane of focus vertically. Pattern recognition is used to detect the components in each individual image and locate their 3-D positions, and we rely on multiple images of the workspace to resolve the rich distribution of components along the Z-direction.

3. Imaging System

3.1 Hardware Setup

Figure 1 shows a schematic diagram of the hardware setup for the 3-D imaging module. The sample cell, which consists of a glass cover slip on a microscope slide with fluid sealed between them containing micro-spheres, is placed on the stage of the microscope (Zeiss Axiotech vario upright microscope with a 63x / 1.40NA Zeiss Plan-Apochromat oil immersion objective). The workspace is defined as a 3-D rectangular region in the sample cell bounded by the glass cover slip and the slide and can be imaged in either transmission or reflection. A Cartesian coordinate frame is defined for the workspace, in which the Z-axis is perpendicular to the substrate of the sample cell. A piezo-electric (PI-721) actuator drives the microscope objective along the Z-direction and thereby changes the microscope's plane of focus. A CCD camera (QImaging Retiga Exi) takes images of the workspace as the plane of focus moves in Z. For convenience, the distance of an object to the microscope's plane of focus will be referred to as the relative z-coordinate of the object, in distinction with the object's absolute z-coordinate.

3.2 Overview of 3-D Imaging Algorithms

Although our current interest is the 3-D imaging of micro-spheres, we develop an infrastructure that can be easily extended to work with other components as well, e.g. nanowires. The function of the 3-D imaging algorithms is to take a stream of image stacks of the workspace and to build a 3-D model of the volume. The algorithms we develop consist of two major steps. The first step is to analyze each image frame individually to extract geometric information about the objects that are visible in that frame. The second step is to combine the information extracted from images into a consistent description of the entire workspace.

The image is first segmented into a number of areas of interest. Each area of interest is a rectangular region that contains one or more objects. The purpose of this step is to identify all the areas of interest in the image so that subsequent operations can concentrate on these regions. This helps to eliminate the processing of the empty regions since typically over three fourths of the image is empty, depending on the density of objects in the workspace. Taking into account the computational overhead introduced by image segmentation, the net gain in speed is generally

over 60%. In addition, subsequent image processing operations can produce more reliable results by limiting them to smaller local regions. In order to identify the areas of interest, an image is first converted to a binary bitmap, in which a pixel with value 1 indicates that it is part of an object. The 1-pixels form a number of connected regions throughout the bitmap, which can be isolated and labeled by a region growing algorithm. An axis-aligned bounding box is then calculated for each isolated connected region and used as an area of interest in the image. Once a number of areas of interest have been selected, they will be sequentially processed by the object detection functions. These functions detect the objects' type, i.e. sphere or wire, and extract the associated geometric information, such as position, dimension and orientation.

After the image frame is segmented, the processing for the second step begins. In this step, the geometric information is extracted and put into a queue. Due to background noise, limited resolution and overlapping of objects, some of the geometric information obtained from a single frame may not be conclusive, such as the Z-positions. However, information from multiple frames can be combined to produce more accurate and reliable estimates. In order to do this, the correspondence of objects from one frame to the next needs to be resolved first, i.e. an object identified in one frame should be correctly linked to its image in the next frame. In the case that the movement of objects from frame to frame is small, e.g. dimension of objects greater than a few microns and images taken at a frame rate greater than 4 frames per second (fps), the positions of objects can be used as a major indicator to resolve this correspondence. In addition, auxiliary information such as the type and dimension of the object can also be used. Once the correspondence of objects is established, geometric information extracted about the same object from multiple frames can be combined.

4. Algorithms for Estimating Positions of Micron-Sized Spheres

4.1 Overview

The algorithms for estimating positions of micro spheres can be described as three major steps and associated sub-steps:

- Identify areas of interest in the image
  - Convert the raw image to a 1-bit bitmap by thresholding
  - Identify connected regions in the threshold bitmap
  - Find an axis aligned bounding box for each connected region

- Locate the XY positions of spheres
  - Compute the gradient field of the raw image in the specified region
  - Transform the gradient field to an accumulation array
  - Locate the XY positions of the peaks in the accumulation array

- Locate the Z positions of spheres
  - Compute the signature curve for each sphere identified in image
  - Estimate the Z depth of a sphere by matching its signature curve to the "standard" signature curves

Detailed description of the algorithms will be given in successive sections.

In our experiments, the spheres used are of uniform diameter. The geometric information of the spheres that we are interested in retrieving are the X, Y and Z coordinates of the center of each sphere.

4.2 Finding Areas of Interest

As mentioned in Section 3, the first step to find areas of interest in the raw image is to convert the image to a binary bitmap, in which pixels representing the objects are marked as 1s and pixels representing the background are marked as 0s. Two methods can be used to accomplish this, gradient thresholding or intensity thresholding. The gradient thresholding method is to compute the gradient field of the image first and then mark all pixels with a gradient magnitude greater than a certain threshold as 1s. It utilizes the fact that the boundaries of the objects have large gradients while the gradients of the background pixels are small. From the many experiments we have conducted, it was also observed that the objects generally have a portion, either the boundary or the central part, that is remarkably brighter or darker than the background. In such cases, the marking of the pixels representing the objects can be done by an intensity thresholding, i.e. all pixels with an intensity value greater than a certain threshold are marked as 1s.

Figure 2 shows an image of glass spheres before and after intensity thresholding, as well as the detected connected components and the corresponding axis-aligned bounding boxes. The advantage of the intensity thresholding method over gradient thresholding is less computation time. However, it is not as good as gradient thresholding in terms of robustness to the variation and nonuniformity of background intensity. For example, as the plane of focus moves along the z direction, the background intensity changes and in turn the threshold value needs to be adjusted accordingly. The background intensity also depends on the lighting conditions. In this case, a calibration process is required to determine the appropriate threshold values for images taken at different positions of the plane of focus a priori.

As can be seen from Figure 2, some of the pixels that belong to objects will not be identified accurately by using either of the thresholding algorithms discussed. However, this will not leave any portion of an object outside the areas of interest. On the other hand, fewer 1-pixels marked for an object can reduce the time required by the region-growing algorithm. The binary bitmap obtained from thresholding generally contains a number of false regions, which contain no object but pixels with extraordinary intensity values. These false regions are generally smaller than true areas of interest and therefore can be easily removed by a size pruning.

4.3 Locating the X-Y Positions of Spheres

As mentioned in Section 2, a straightforward method to compute the X-Y position of an object in image is to first identify the pixels that belong to that object and then compute the centroid of those pixels. A popular and simple way to identify pixels of an object is by intensity thresholding and separation of the connected components. However, this method does not work for objects that are partially visible or objects that are clustered together. In the former case, the centroid of

pixels might not be the center of the object. In the latter case, there is no easy way to separate pixels that belong to one object from pixels that belong to another object.

Observe that the image of a micro-sphere has a pattern of concentric rings (see Figure 3) due to diffraction. We used an algorithm based on circle detection to locate the X-Y positions of the spheres. A popular algorithm for detecting circular patterns in image is the Circular Hough Transform or its variations. We adopted the algorithm proposed by Illingworth [Illi87] and made a few modifications to accommodate our application. The algorithm is explained below in detail.

First, the gradient field of image intensity in an area of interest is computed using the following equation:

$$\nabla I(i,j) = (V_x, V_y)\,|_{(i,j)} = \big(I(i,j) - I(i,j-1), I(i,j) - I(i-1,j)\big) \qquad (1)$$

where (i,j) are the pixel indices, $\nabla I(i,j)$ is the gradient vector at pixel (i,j), which consists of x- and y-component, and $I(i,j)$ is the image intensity at pixel (i,j).

Due to the concentric ring pattern of a micro-sphere's image, the non-zero gradient vectors in the gradient field are either pointing towards the center of a sphere or away from it. By taking advantage of this feature, a transform is defined to convert the gradient field to an accumulation array, in which the pixel intensity corresponds to the probability of that pixel being the center of a sphere. The maximum intensity in the accumulation image represents the center position of a sphere. The accumulation array is usually selected to have the same dimension as the gradient field. The construction of the accumulation array is done by a voting process as follows (see Fig. 8): For each non-zero gradient vector $\nabla I(i,j)$ in the gradient field, a weight value is added to the pixels in the accumulation array that lie on the line segment defined by the vector $\nabla I(i,j)$. The length of the line segment is set to be the possible maximum diameter of the spheres (in pixels) and the magnitude of $\nabla I(i,j)$ is used as the weight value. After collecting the votes from all non-zero gradient vectors, the accumulation array is constructed. In Fig. 8, the darkest pixel has the maximum weight. Figure 5 shows the gradient field of an image of clustered glass spheres and the corresponding accumulation array.

For an area of interest in an image that contains multiple spheres, the corresponding accumulation array will have multiple peaks as well. The detection of peaks in the accumulation array is done by the following process:

Step 1: A Laplacian of Gaussian (LoG) filter is applied to the accumulation array. The LoG filtering can fill the transition areas between local peaks with negative values or zeros, which makes it easier to separate the peaks in the successive steps.

Step 2: The accumulation array is thresholded with a positive value (25% of the maximum intensity in the accumulation array after LoG filtering). The local peaks in the accumulation array, as well as their close neighborhood, are marked as 1s. The rest of the image is marked as 0s, which keeps the local peaks isolated from each other.

Step 3: The isolated regions with local peaks are detected by a region growing algorithm. The weighted centroid of an isolated region is taken as the location of the local peak it encloses.

Each local peak in the accumulation array corresponds to a detected sphere in the image. The computed positions of local peak are then converted to positions in the image, which are taken as the center positions of the spheres detected.

4.4 Estimation of the Z-Coordinates

4.4.1 Definition of Signature Curves

The image of a micro-sphere exhibits different patterns when located at different distances from the microscope's plane of focus. This can be verified by taking an image stack of a stationary microsphere. A set of such images of a glass sphere is shown in Figure 8. As we pass through sections of the glass sphere at different z-depths, the image first shows multiple concentric rings patterns and then gradually changes to a pattern with a single dominant ring. At one point the single-ring pattern of the glass sphere is the sharpest and then the pattern blurs and eventually becomes a faint cloud (not shown in the Figure). The image pattern of a micro-sphere may also depend on the lighting conditions.

In order to resolve the Z-coordinate of the micro-sphere from its image pattern, we define a discrete signature curve $f(r)$ over the gradient field of the sphere's image, where r is the distance to the center position of the sphere and $f(r)$ is the averaged dot product of the gradient vector and the radial vector. A mathematical description of this definition is the following.

Let (i_C, j_C) be the center position of a detected sphere in the image (see Figure 6). For a pixel (i, j) in the neighborhood of (i_C, j_C), let $\vec{V}(i, j)$ be the gradient vector of the pixel (i, j) and $\vec{q}(i, j)$ be the vector from (i_C, j_C) to the center of pixel (i, j). A sequence of discrete r values with fixed interval are selected, which represent distances to the sphere center (i_C, j_C). For each r value, $f(r)$ is defined using the following equation

$$f(r) = \frac{\sum_{(i,j)} \left[\vec{V}(i, j) \cdot \vec{q}(i, j) / \left\| \vec{q}(i, j) \right\| \right]}{\sum_{(i,j)} 1} \qquad (2)$$

where the summation is over all pixels (*i*,*j*) that satisfy

$$\left| \left\| \vec{q}(i, j) \right\| - r \right| < \frac{\Delta r}{2} \qquad (3)$$

where Δr is the interval between adjacent r values.

Figure 7 shows an example of a glass sphere's image, the gradient field and the corresponding signature curve. As we can see, the signature curve effectively extracts the intensity change of the image pattern along the radial direction. By defining the curve based on the gradient field of the image instead of the image intensity, we eliminate the influence of variable background

intensity in the image. We also take advantage of the circular symmetry of the image pattern and get the signature value at each r averaged along the tangent direction. Figure 8 shows few representative signature curves corresponding to the image patterns of the glass sphere at different distance from the plane of focus.

4.4.2 Using an Image Mask for Clustered Spheres to Reduce Error in Signature Curves

The computation of a signature curve for a detected sphere is performed over the surrounding region of the estimated center position of the sphere, C_i. For an isolated sphere, this region is a square centered at C_i with a side length slightly larger than the diameter of the sphere. However for a sphere that is clustered with other sphere(s), the selection of a region for computation is more complicated. Overlapping regions with other sphere(s) must be avoided for they may distort the signature curve. In order to solve this problem, we build a bitmap mask on top of the square region for each clustered sphere to block the overlapping part. For an area in which all spheres have been resolved, these masks can be constructed automatically. Figure 9 shows an example of such masks and a signature curve that was built with and without the mask. As can be seen from the figure, the use of mask prevented the distortion to the signature curve.

4.4.3 Using Signature Curves to Estimate Z-Coordinates

As mentioned before, the image pattern of a micro-sphere depends not only on its relative z-coordinate, i.e. the distance from the sphere to the microscope's plane of focus, but also on other factors such as the lighting conditions. However, for a fixed experiment setup and a single type of micro-sphere, the shape of the signature curve is determined solely by the sphere's relative z-coordinate, although it may be deformed a little by background in the image. In order to estimate the relative z-coordinate of the micro-sphere from its signature curve, we developed an algorithm consisting of the following steps:

- For each experimental setup, i.e. microscope, lighting conditions and sphere material, a set of calibration signature curves are acquired by taking images of a stationary sphere at a number of z-positions. Figure 8 shows a set of calibration signature curves.

- When resolving a 3-D scene of microspheres at run-time, a signature curve is computed for each sphere detected in the image. This signature curve is then matched against the calibration curve set based on a least square error measure. The relative z-coordinate of the standard signature curve with the best match is chosen as the relative z-coordinate of the sphere. A mathematical description of this is given below.

  Denote the calibration signature curves as $Y_k(r)$, where k = 1, …, K represents the curve for different positions of the plane of focus. For a signature curve $y(r)$ acquired at run-time, the residual of the least square fitting of $y(r)$ to each of Y_k is computed, i.e.

  $$e_k = \sum_{r=d_1}^{r=d_N} \left[y(r) - s_k \cdot Y_k(r) \right]^2 \qquad (4)$$

  where $[d_1, d_N]$ is the range for variable r, e_k is the residual and s_k is the amplitude scalar that gives the minimum e_k for each k. The reason for introducing the scalar s_k into the

evaluation of residual is because, although the shape of the signature curve is determined by the sphere's relative z-coordinate, its amplitude may vary due to the change of the overall image intensity.

Z values corresponding to a residual e_k which is less than a predetermined threshold are selected, and in some cases multiple z values may qualify.

- The Z-coordinate of the sphere is calculated by adding its relative z-depth to the Z-coordinate of the plane of focus when the image was taken.

4.4.4 Combining the Estimates of Z-Coordinate from Adjacent Frames

As discussed above, the estimation of a glass sphere's Z-coordinate from a single image frame may yield two possible values. However, by combining the estimates from two adjacent frames, such ambiguity can be eliminated. Here we assume that the movement of a sphere during the interval of two frames being taken is very small, which is true under our conditions for particles with a diameter greater than or equal to 1 micron.

We used a confidence number to describe the uncertainty in the Z-coordinate estimation. This number is determined by the residual of the matching signature curves and whether there are multiple possible matches. If the residual is large and/or there is more than one likely match, the confidence number will be small and estimations from adjacent frames will be combined to obtain a more accurate estimation.

4.5 Updating Workspace Status in Real-Time

The assembly process using optical tweezers requires constructing the 3-D scene of the workspace in real-time. The dominant motion of the components in the workspace, besides being manipulated by the optical traps, is the Brownian motion in the fluid. Therefore, to achieve real-time performance the 3-D scene must be updated fast enough to track the motion of the particles. In practice, the optical tweezers instrument is reasonably tolerant to error in the position estimate and can grasp components that are within a few diameters of the trap. Based on our experience on manipulating micro-spheres by using optical tweezers, we set our initial goal of updating the workspace at 20 times per second.

As mentioned in Section 3.1, the imaging system's plane of focus is moved up and down to scan the workspace vertically. In each image, only objects in a limited portion of the workspace are in focus and hence only the geometric information of these objects can be extracted out of that frame. As a result, for each image only part of the workspace can be reliably updated. This refreshing scheme works in a similar way as a radar screen does, in which only a sector gets updated at a time but as the scanning takes place circularly the whole disk gets updated over a period of time.

5 Computational Experiments

5.1 Verification of the Algorithm for Z-Coordinate Estimation

The algorithm for locating the X-Y positions of spheres can be verified easily. Marks representing the calculated center positions of spheres can be drawn on top of the raw image to check the position accuracy and whether there are missing or false detections. On the other hand, the verification of the position accuracy along Z-axis is not as straightforward since there is no convenient way to measure the Z-coordinates of the spheres directly.

We therefore developed the following scheme to examine the accuracy of the Z-coordinate estimation. Micro-spheres are allowed to settle to the bottom of the assembly cell until they stick to the bottom surface and remain motionless. An image stack of these spheres is taken by moving the plane of focus from the bottom to the top of the observed volume. One sphere in the image stack is selected and a set of signature curves is computed from its patterns to be the standard signature curves. Then the standard curve set is used to estimate the relative Z-coordinates of the rest of the spheres. The tilt of the bottom surface with respect to the optical axis can also be estimated, and usually amounts to less than a few microns over the field of view. The error in the estimated Z-coordinates can then be calculated.

We conducted this test on silica micro-spheres with two different sizes, 0.97μm and 2.47μm, and 3 different illumination intensities. For the 0.97μm spheres, a stack of 11 images were used to acquire the calibration signature curves. For the 2.47μm spheres, 19 images were used. In both cases, the Z-coordinate interval between two consecutive image frames is 0.1μm. Under each test condition, at least 4 spheres were selected randomly to study the accuracy of Z-coordinate estimation. Figure 10 shows the estimation result of a 2.47μm sphere by using the calibration signature curves obtained under the same illumination condition. The X-axis represents the position of the microscope's plane of focus at each step in the series, and the Y-axis gives the estimated Z-coordinate of a sphere relative to the plane of focus. As can be seen from the figure, the estimated Z-coordinates are very close to the true values. Figure 11 shows the experiment results for the 0.97μm spheres. Table 1 shows the maximum and root mean square (RMS) of estimation errors for 0.97μm and 2.47μm spheres under different illumination intensities. For all cases, the calibration signature curves used for estimation are curves obtained by using spheres with the same size and under the same illumination intensity. On average, the maximum error of the estimated Z-coordinates is around 0.06μm and the RMS error is about 0.022μm. Given that the radius for a particle to be captured into the trap is on the order of the particle diameter, these errors are at least an order of magnitude better than required to guide the optical tweezers to trap the spheres – the objective of this work.

We also estimated the Z-coordinates of spheres by using calibration signature curves that were obtained under different illumination conditions. Figure 12 shows the estimated Z-coordinates of a 0.97μm sphere under low illumination by using calibration signature curves that were obtained under low, medium and high illumination intensities. As can be seen from the figure, the estimated values given by the calibration data obtained under low and medium illumination intensities are very close to true values, while the estimated values corresponding to the calibration data obtained under high illumination intensity have a larger error. Figure 13 shows the results of the 2.47μm spheres. Table 2 and 3 show the maximum and RMS error of the estimated Z-coordinates under different illumination intensities. We believe the reason for getting large estimation error when using calibration data obtained under dramatically different

illumination intensity is that, the image pattern of a silica sphere changes significantly as the illumination intensity of the microscope changes.

5.2 Overall Performance of the Algorithms

The 3-D imaging scheme and algorithms have been tested over a variety of experimental setups, i.e. different materials of spheres (glass and silica), different sphere sizes (0.97μm and 2.47μm), different lighting methods (transmission and reflection) and illumination intensities. The reconstructed 3-D scene of the workspace can be displayed using OpenGL based rendering for convenient diagnosis. Figure 14 shows a raw image of spheres in the workspace and the rendering of the resolved 3-D scene.

The developed algorithms are able to resolve closely clustered spheres. As shown in Figure 15, individual spheres can be detected correctly even though the image has occlusions. This is enabled by using the image masks described in Section 4.4.2. For images that have severe occlusions (such as the right two figures in Figure 15), the majority of spheres can still be detected correctly, although false or missing detections may happen occasionally. The optical sectioning method and the Z-coordinates estimation algorithm work very well to resolve the distribution of spheres along the imaging direction. Figure 16 shows a sequence of images of 4 clustered spheres (one sphere on top of the other three). As the plane of focus moving up, the 3 spheres underneath gradually fade out and the sphere on top appears. From any single image, the positions of the 4 spheres can not be resolved, but by using the optical sectioning based method this situation can be resolved successfully.

5.3 Computation Speed of the Algorithms

The 3-D imaging algorithms were implemented in C++. To meet the goal of processing 20 frames per second, special attention was paid to optimize the computation speed of the algorithms, e.g. the use of SIMD (Single Instruction Multiple Data) instructions in the code. On a laptop PC (Pentium M 1.6GHz, 64K L1 cache and 1024K L2 cache, 100MHz Front Side Bus, 512MB DDR-SDRAM) running Windows, the developed software is able to reach a processing speed of 24 ms/frame (equivalently over 40 frames per second) on images with 618×518 pixels resolution and 8-bit grayscale depth. The number of spheres in each image is around 60.

6. Conclusions

This paper describes algorithms for estimating positions of micro-spheres. Our results indicate that these algorithms are sufficiently efficient and capable of providing the desired frame-rates. Moreover, these algorithms are able to work with the expected levels of noise and distortions in the images and produce accurate enough estimates for optical tweezers applications. Our results also indicate that these algorithms are capable of resolving closely clustered micro-spheres.

We are developing these algorithms to provide the basic foundations for realizing automated assembly operations at the μm and nm scales using optical-tweezers, and to implement a reliable, efficient, and autonomous assembly process for fabricating micro-spheres based devices and structures. These capabilities can be useful in microsphere applications ranging from colloid

studies, to cell sorting, to manipulation of single molecules tethered to glass beads. We expect that the envisioned assembly cell will enable researchers to explore new design possibilities in areas such as biomedical, material science, and MEMS. Automated assembly capability will allow exploration of a large number of design options in a cost effective manner.

In the near future we plan to extend our algorithms in the following three different areas. First, we plan to extend our algorithms to work with metallic particles. Metallic particles are expected to produce different types of images and hence new signature curves will need to be developed to handle these cases. Second, we plan to extend the algorithms to work with the cases where particles move significantly between two successive images. This will require us to develop new method for aggregating predicted locations in 3D space and resolve ambiguities. Finally, we plan to extend the algorithms to work with nanowires. This will require us to develop more general signatures.

Acknowledgments. The authors gratefully acknowledge the support provided by the Center for Nano Manufacturing and Metrology, a joint venture between the University of Maryland and the National Institute of Standards and Technology. Commercial product or company names in this paper are given for informational purposes only. Their use does not imply recommendation or endorsement by the National Institute of Standards and Technology or the University of Maryland.

References

[Agar05] Agarwal, R., Ladavac, K., Roichman, Y., Yu, G. H., Lieber, C. M., Grier, D. G. Manipulation and assembly of nanowires with holographic optical traps. *Optics Express*, 13(22):8906-8912, 2005.

[Ashk86] Ashkin, A., Dziedzic, J. M., Bjorkholm, J. E., Chu, S. Observation of a single-beam gradient force optical trap for dielectric particles. *Optics Letters*, 11(5):288-290, May 1986.

[Ashk00] Ashkin, A. History of optical trapping and manipulation of small-neutral particle, atoms, and molecules. *IEEE Journal Of Selected Topics In Quantum Electronics*, 6 (6): 841-856 Nov-Dec 2000.

[Bali05] A. Balijepalli, T.W. Lebrun, and S.K. Gupta. A flexible system framework for a nanoassembly cell using optical tweezers. *ASME Computers and Information in Engineering Conference*, Philadelphia, Pennsylvania, USA, September 2006.

[Brak89] Brakenhoff, G.J., Vandervoort, H.T.M., Vanspronsen, E.A., et al. 3-dimensional imaging in fluorescence by confocal scanning microscopy. *Journal of Microscopy-Oxford*, 153:151-159 Part 2, 1989.

[Clen02] Clendenon, J.L., Phillips, C.L., Sandoval, R.M., et al. Voxx: a PC-based, near real-time volume rendering system for biological microscopy. *American Journal of Physiology - Cell Physiology*, 282(1):C213-C218, 2002.

[Croc96] Crocker, J.C., Grier, D.G. Methods of digital video microscopy for colloidal studies. *Journal of Colloid and Interface Science*, 179(1):298-310, 1996.

[Fred99] Fredrich, J.T. 3D imaging of porous media using laser scanning confocal microscopy with application to microscale transport processes. *Physics and Chemistry of the Earth Part A - Solid Earth and Geodesy*, 24(7):551-561, 1999.

[Gorm05] Gorman, J. J., Lebrun, T. W., Balijepalli, A., Gagnon, C., and Lee, D. Characterization of optical traps using on-line estimation methods. In *Proceedings of the Optics and Photonics*, San Diego, 2005.

[Illi87] Illingworth, J., Kittler J. The adaptive Hough Transform. *IEEE Transactions on Pattern Analysis and Machine Intelligence*, 9(5):690-698, 1987.

[Luca96] Lucas, L., Gilbert, N., Ploton, D., et al. Visualization of volume data in confocal microscopy: comparison and improvements of volume rendering methods. *Journal of Microscopy – Oxford*, 181:238-252 Part 3, 1996.

[Pauz06] Pauzauskie, P. J., Radenovic, A., Trepagnier, E., Shroff, H., Yang, P. D., Liphardt, J. Optical trapping and integration of semiconductor nanowire assemblies in water. *Nature Materials*, 5(2):97-101, 2006.

[Svob94] Svoboda, K., Block, S. Optical trapping of metallic Rayleigh particles. *Optics Letters*, 19(13):930-932, 1994.

[Yu04] Yu, T., Cheong F. C., Sow C. H. The manipulation and assembly of CuO nanorods with line optical tweezers. *Nanotechnology*, 15(12):1732-1736, 2004.

[Week00] Weeks, E.R., Crocker, J.C., Levitt, A.C., et al. Three-dimensional direct imaging of structural relaxation near the colloidal glass transition. *Science*, 287(5453):627-631, 2000.

[Wils89] Wilson, T. Optical sectioning in confocal fluorescent microscopes. *Journal of Microscopy-Oxford*, 154:143-156 Part 2, 1989.

Figure Captions

Figure 1. Schematic diagram of the imaging module (figure not to the scale)

Figure 2. Image segmentation

Figure 3. The ring (or concentric rings) pattern of the images of micro spheres

Figure 4. Construction of the accumulation array from the gradient field

Figure 5. Gradient field of clustered spheres and the corresponding accumulation array

Figure 6. Definition of signature curve of the image pattern of a glass sphere

Figure 7. Example of signature curve computed from an image of a glass sphere

Figure 8. Signature curves of a glass sphere at different z-depths

Figure 9. Using mask in the computation of signature curve

Figure 10. Estimated Z-coordinates of a 2.47μm sphere by using calibration signature curves obtained under the same illumination condition

Figure 11. Estimated Z-coordinates of a 0.97μm sphere by using calibration signature curves obtained under the same illumination condition

Figure 12. Estimated Z-coordinates of a 0.97μm sphere (under low illumination intensity) by using calibration signature curves obtained under different illumination intensities

Figure 13. Estimated Z-coordinates of a 2.47μm sphere (under medium illumination intensity) by using calibration signature curves obtained under high and medium illumination intensities

Figure 14. Reconstructed 3-D scene of glass spheres

Figure 15. Resolving clustered spheres

Figure 16. Resolving spheres overlapping in Z-direction

Tables

	2.47μm sphere, high illumination	2.47μm sphere, medium illumination	2.47μm sphere, low illumination	0.97μm sphere, high illumination	0.97μm sphere, medium illumination	0.97μm sphere, low illumination
Max. Error (μm)	0.055	0.056	0.062	0.060	0.048	0.069
RMS Error (μm)	0.018	0.018	0.024	0.026	0.022	0.025

Table 1. Error in the estimated Z-coordinates of spheres under different illumination intensities

	Calib. data obtained at low illumination	Calib. data obtained at medium illumination	Calib. data obtained at high illumination
Max. Error (μm)	0.056	0.043	0.100
RMS Error (μm)	0.023	0.020	0.037

Table 2. Error in the estimated Z-coordinates of a 0.97μm sphere (under low illumination intensity) by using calibration signature curves obtained under different illumination intensities

	Calib. data obtained at medium illumination	Calib. data obtained at high illumination
Max. Error (μm)	0.056	0.071
RMS Error (μm)	0.020	0.027

Table 3. Error in the estimated Z-coordinates of a 2.47μm sphere (under medium illumination intensity) by using calibration signature curves obtained under different illumination intensities

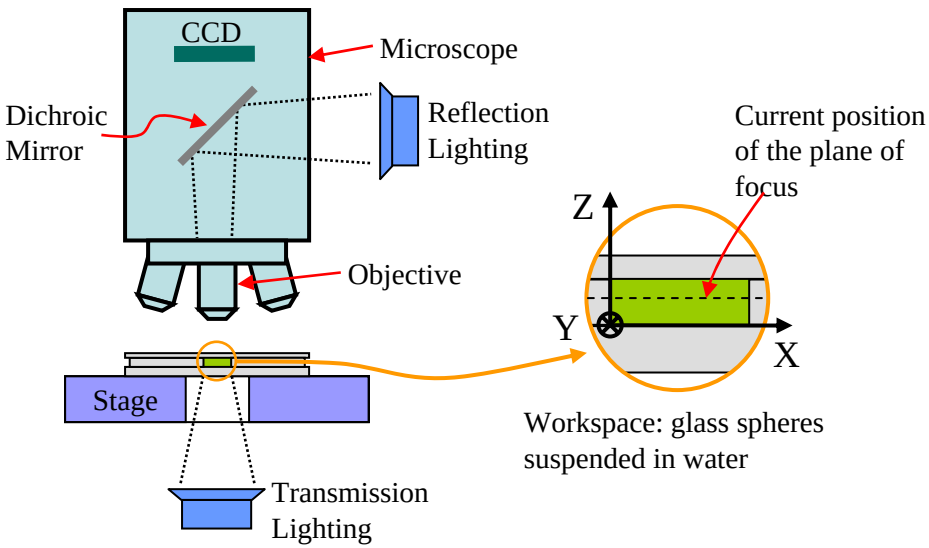

Figure 1. Schematic diagram of the imaging module (figure not to the scale)

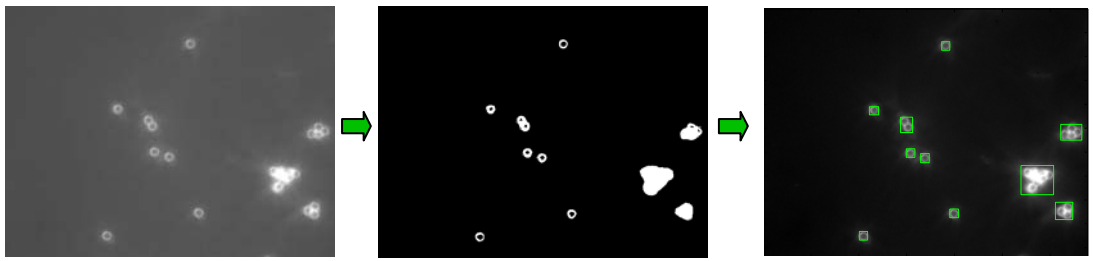

Figure 2. Image segmentation

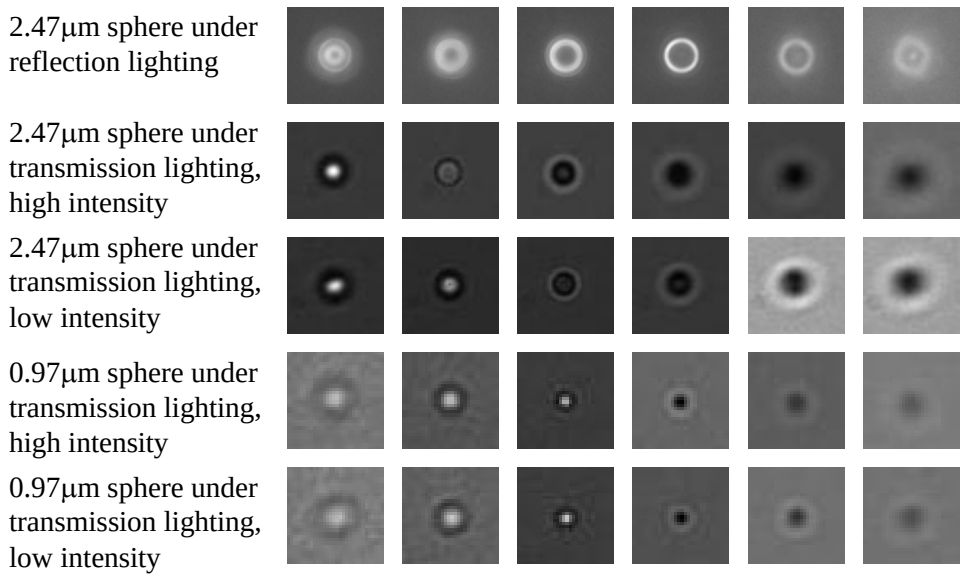

Figure 3. The ring (or concentric rings) pattern of the images of micro spheres

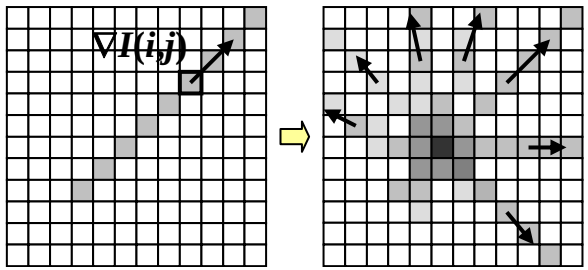

Figure 4. Construction of the accumulation array from the gradient field

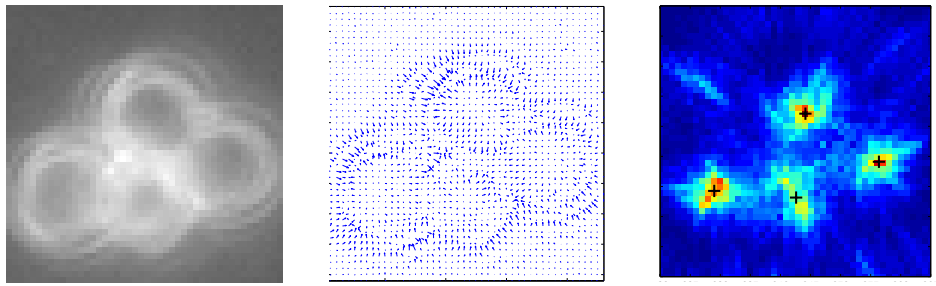

Raw image | Gradient field | Accumulation array in pseudo-color

Figure 5. Gradient field of clustered spheres and the corresponding accumulation array

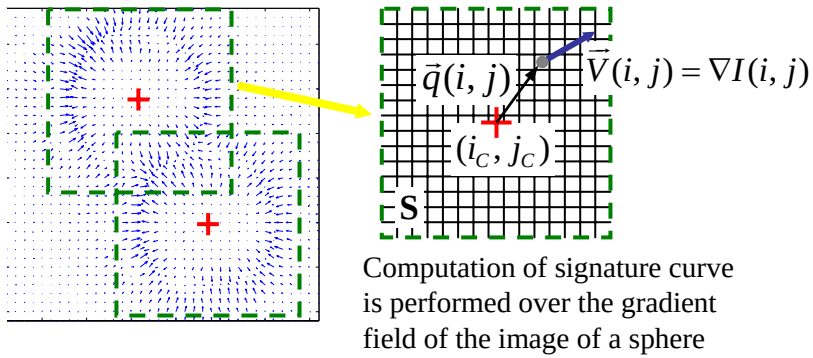

Figure 6. Definition of signature curve of the image pattern of a glass sphere

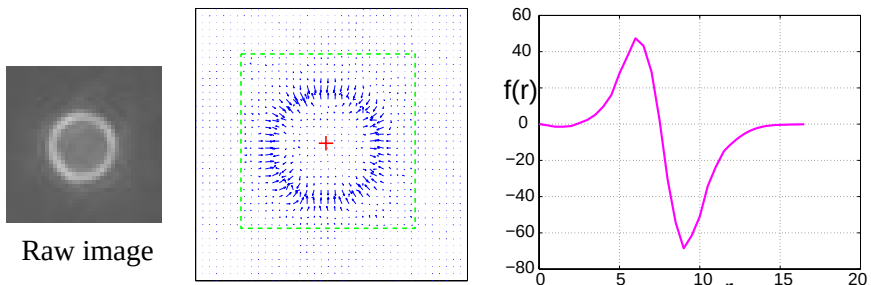

Figure 7. Example of signature curve computed from an image of a glass sphere

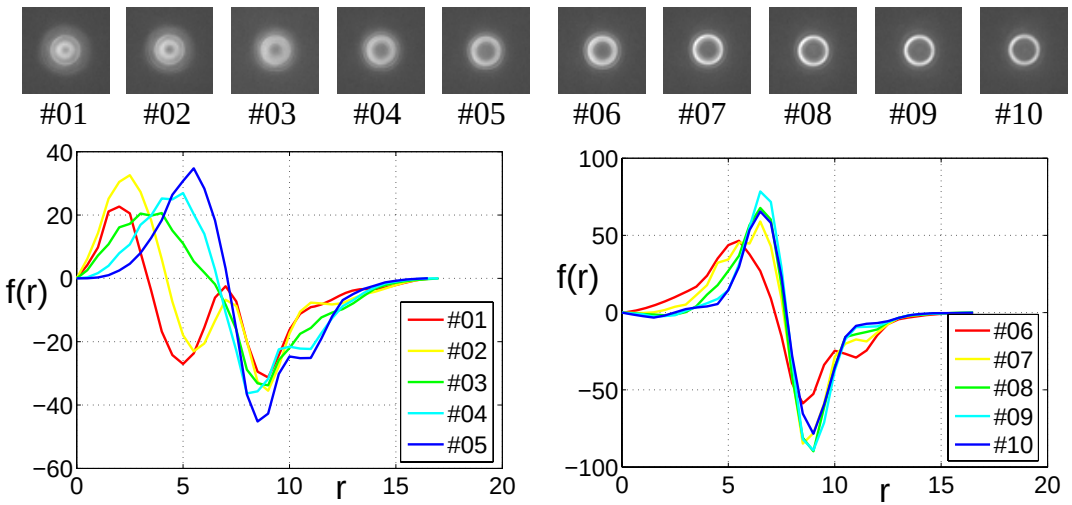

Figure 8. Signature curves of a glass sphere at different z-depths

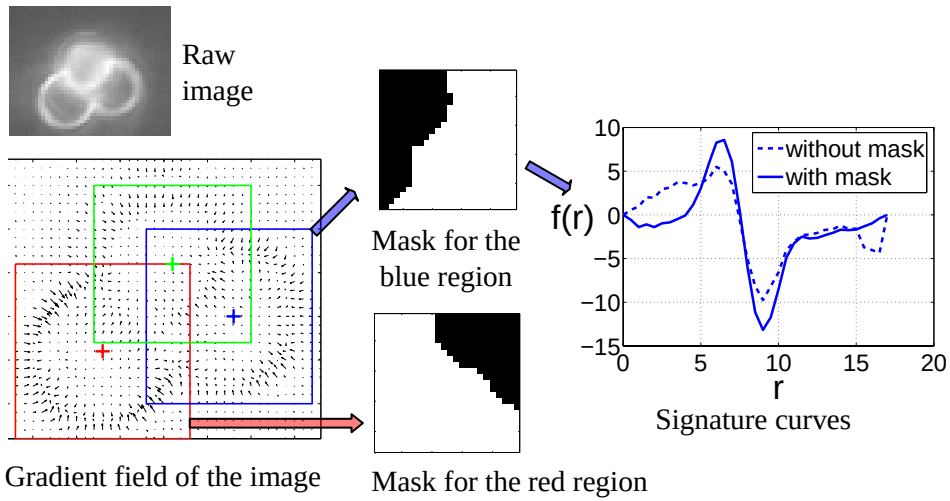

Figure 9. Using mask in the computation of signature curve

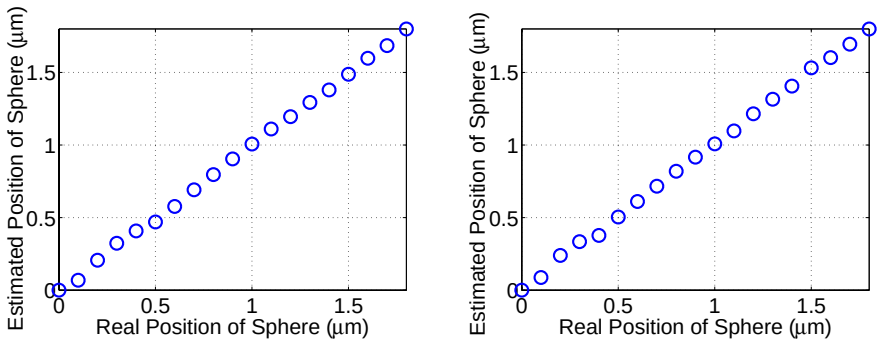

a) High illumination intensity b) Medium illumination intensity

Figure 10. Estimated Z-coordinates of a 2.47μm sphere by using calibration signature curves obtained under the same illumination condition

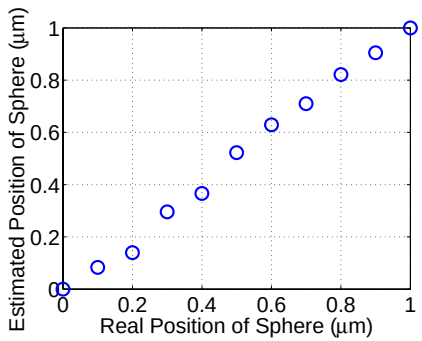

a) High illumination intensity

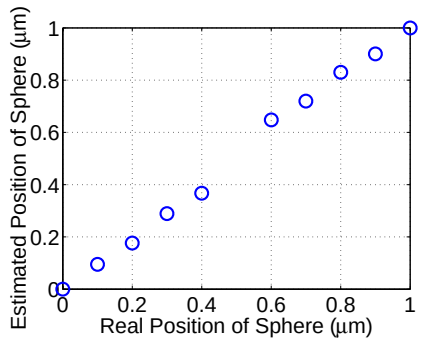

b) Medium illumination intensity

Figure 11. Estimated Z-coordinates of a 0.97μm sphere by using calibration signature curves obtained under the same illumination condition

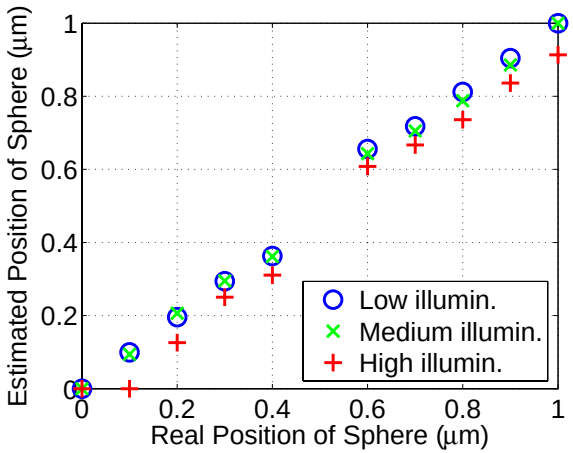

Figure 12. Estimated Z-coordinates of a 0.97µm sphere (under low illumination intensity) by using calibration signature curves obtained under different illumination intensities

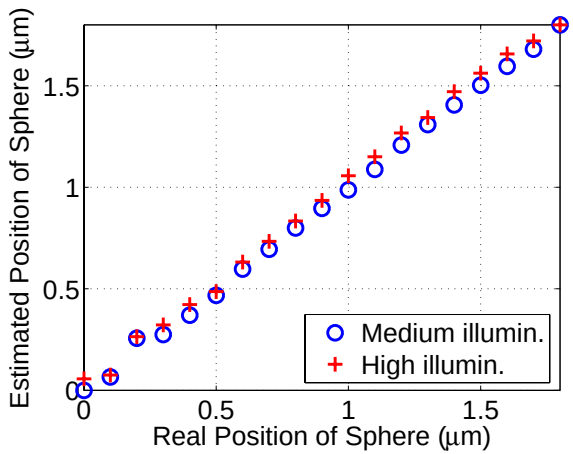

Figure 13. Estimated Z-coordinates of a 2.47µm sphere (under medium illumination intensity) by using calibration signature curves obtained under high and medium illumination intensities

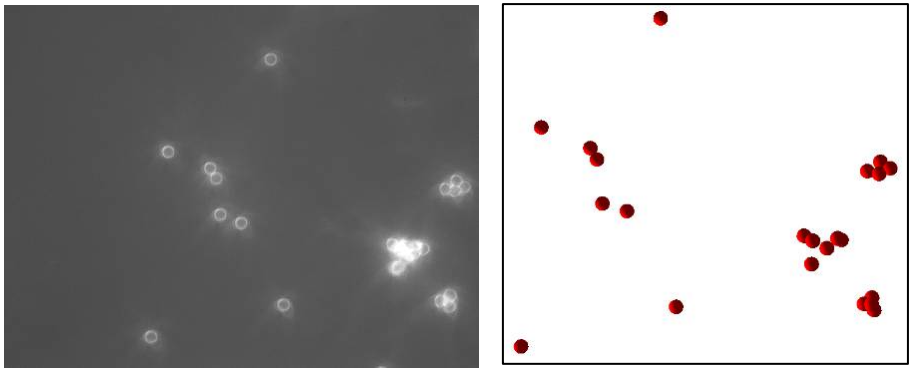

One of the raw images in the stack

Reconstructed scene

Figure 14. Reconstructed 3-D scene of glass spheres

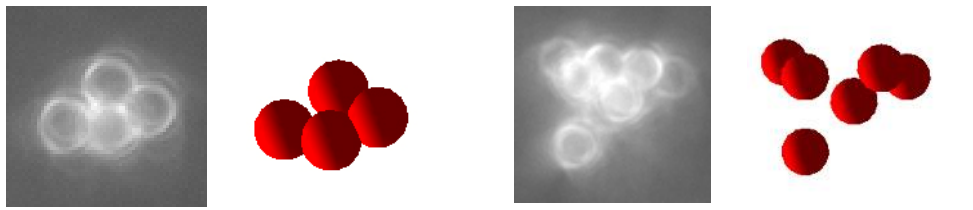

Portion of a raw image | Rendering of the reconstructed scene | Portion of a raw image | Rendering of the reconstructed scene

Figure 15. Resolving clustered spheres

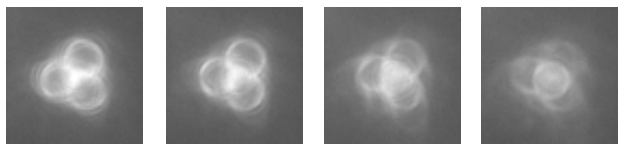

Figure 16. Resolving spheres overlapping in Z-direction